An engineered anisotropic nanofilm with unidirectional wetting properties

Niranjan A. Malvadkar[1][†], Matthew J. Hancock[2][†], Koray Sekeroglu[1], Walter J. Dressick[3] and Melik C. Demirel[1]*

Anisotropic textured surfaces allow water striders to walk on water, butterflies to shed water from their wings and plants to trap insects and pollen. Capturing these natural features in biomimetic surfaces is an active area of research. Here, we report an engineered nanofilm, composed of an array of poly(*p*-xylylene) nanorods, which demonstrates anisotropic wetting behaviour by means of a pin-release droplet ratchet mechanism. Droplet retention forces in the pin and release directions differ by up to 80 μN, which is over ten times greater than the values reported for other engineered anisotropic surfaces. The nanofilm provides a microscale smooth surface on which to transport microlitre droplets, and is also relatively easy to synthesize by a bottom-up vapour-phase technique. An accompanying comprehensive model successfully describes the film's anisotropic wetting behaviour as a function of measurable film morphology parameters.

Anisotropic textured surfaces have direction-dependent properties that provide the basis for such diverse functions as gecko[1] and water strider locomotion[2], butterfly wing water repellency[3] and plant pollination[4]. In each case, such surfaces usually comprise millions of organized structures per square millimetre, often at multiple roughness scales, with direction-dependent geometrical features that produce directionally dependent wetting or adhesion. For example, certain butterfly wings have overlapping microscales with nanotips that force water droplets to move along the wings away from the insect's body[3]. Engineering synthetic materials with such anisotropic adhesive properties has led to advances in digital microfluidic devices[5,6] and medicine[7,8].

The anisotropic wetting properties of existing engineered surfaces are derived either from spatial gradients (for example, temperature, surface chemistry, morphology)[9–12] or asymmetric asperities[13]. For spatial gradient-based fluidic pathways, droplet motion occurs over a limited range before sticking occurs. In contrast, surfaces with asymmetric asperities do not limit travel distance because no change in the drop's mean free energy occurs for motion in the preferred direction. Anisotropic surfaces with microscale ratchet-like features have been engineered to transport drops in this manner[14–16], although no such surfaces have been synthesized with nanoscale ratchets. Mechanical, thermal or electrical energy were added to induce drop motion; the anisotropic surface determined the direction of motion. In some cases, hydrophobic isotropic nanoscale roughness was added to reduce friction, although the anisotropy was strictly the result of microscale features. In only one case the difference in the droplet retention forces in and against the direction of preferred motion was measured: ∼4.4 μN for 5 μl droplets[16]. In all cases, significant droplet oscillation and deformation occurred during motion. Smaller scale roughness should require less vibrational energy for drop motion, leading to a smoother ride for drops (Supplementary Videos). Moreover, smaller scale roughness should allow smaller drops to be transported, reducing the amount of reagent required for experiments.

We present herein an engineered hydrophobic surface deriving its anisotropic adhesive wetting directly from its asymmetric nanoscale roughness. Special features of our nanofilm include a microscale smooth surface for microlitre droplet transport (Supplementary Videos). Compared with existing drop transport systems, minimal drop shape deformations are noted in our systems for moving drops during transport. Our nanofilm consists of an array of poly(*p*-xylylene) (that is, parylene or PPX) nanorods fabricated using a bottom-up vapour-phase technique, oblique angle polymerization (OAP). OAP involves vaporization and pyrolysis of a *p*-cyclophane precursor to generate a diradical vapour flux (Fig. 1a) using available commercial systems. The flux is directed at a controlled shallow angle onto a substrate, where surface diffusion, in combination with deposition geometry, leads to shadowing and selective growth of anisotropic structures during polymerization[17]. PPX nanofilms have been functionalized to form composites with metals[18,19] and ceramics[20] exhibiting unique properties, such as mechanical anisotropy[17], catalytic activity[21] and enhanced activity for surface Raman spectroscopy[22]. Figure 1b shows the cross-section of a PPX nanofilm of ∼150-nm-diameter nanorods fabricated by OAP of dichloro-[2,2]-*p*-cyclophane (R = Cl in Fig. 1a). We point out that other PPX nanorod films synthesized with hydrophilic groups[23] (for example, R = −CH(OH)CF₃) promote water penetration into the interstitial regions between nanorods, leading to droplet impalement that renders the surfaces impractical for droplet transport applications.

Although counterintuitive, surfaces that exhibit high water contact angles may also exhibit adhesive wetting. For example, the equilibrium contact angles on butterfly wings have been measured above 150°, yet water drops may adhere to the wings even when vertical[3]. High static contact angles are also often associated

[1]Department of Engineering Science and Materials Research Institute, Pennsylvania State University, University Park, Pennsylvania 16802, USA, [2]Department of Medicine, Brigham and Women's Hospital, Harvard Medical School, Boston, Massachusetts 02115, USA, [3]Naval Research Laboratory, Code 6910, 4555 Overlook Avenue, S.W., Washington, District of Columbia 20375, USA. [†]These authors contributed equally to this work. *e-mail: mdemirel@engr.psu.edu.
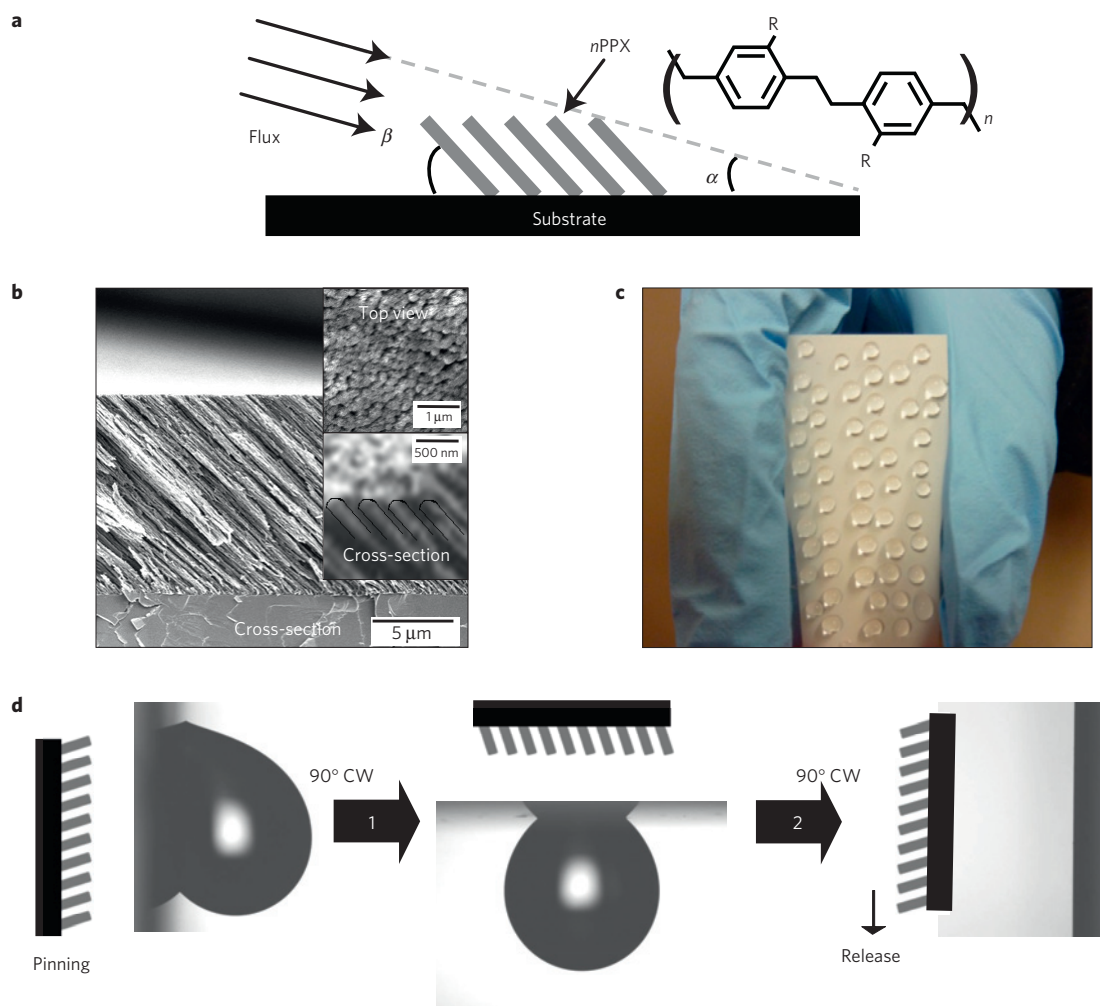
Figure 1 | An overview of PPX nanofilm preparation and anisotropic wetting property. a, Schematic of PPX nanofilm deposition by OAP. **b**, Electron microscope cross-section of PPX nanofilm (insets show top view and high-resolution cross-section micrographs). **c**, Picture of the anisotropic adhesive wetting surface with water drops. **d**, Water adhesion and release in three configurations of the nanofilm. Schematics illustrate the nanorod inclination at each tilt angle and correspond to photographs showing the anisotropic wetting behaviour of the nanofilm.

with nanopore or nanorod arrays, yet these surfaces can also be adhesive[24,25]. The adhesive force of textured hydrophobic surfaces is derived from contact line pinning on asperities[26] and is associated with the extent of the range of contact angles admitted by a surface. Static contact angles lie in a finite range, known as contact angle hysteresis, bounded above and below by the advancing and receding contact angles[9]. An important consequence of hysteresis is a concomitant force of retention F_r that causes droplets to adhere to surfaces; differences in contact angles around the drop perimeter may result in a net contact force that resists drop motion[27,28]. The droplet retention force is estimated by $F_r = k\gamma R(\cos\theta_r - \cos\theta_a)$, where $2R$ is the drop width and k is a pre-factor depending on the contact line shape[27,28]. Contact angle hysteresis has its origins in the pinning of contact lines by microscopic surface irregularities[29], such as surface roughness, contamination and solutes in a liquid[9,30].

The anisotropic adhesive wetting behaviour of our PPX nanofilm is illustrated in Fig. 1c,d. Although water contact angles as high as 120° are observed, water droplets adhere to the surface even when tilted vertically with nanorods pointing up (the pinning position, Fig. 1d, left) or inverted (Fig. 1d, step 1, middle). In the inverted position, the nanofilm surface supports water droplets up to volumes of ∼40 ± 5 µl. When the nanofilm surface is positioned vertically with the nanorods pointing down (the release position, Fig. 1d, step 2, right), the maximum droplet volumes supported

are much lower (Fig. 2). This pin–release behaviour confirms the strong anisotropic wetting response of the film relative to the orientation of the nanorods.

The maximum droplet volume that our inverted nanofilm may support depends on the static load-bearing capability of the inverted nanofilm and the stability of the droplet and its contact line. The static load-bearing capability is estimated as the maximum surface tension force imparted by the PPX nanofilm, $\sim N\pi\gamma d$, where N is the number of columns per unit area (40 million mm^{-2}), γ is the surface tension of water (72 dyn cm^{-1}) and d is the column diameter (∼150 nm) (Supplementary Fig. S1). For our PPX film, the resulting net surface tension force is immense (∼1 N mm^{-2}). As N is proportional to $1/d^2$, the load-bearing capacity is inversely proportional to rod diameter. Therefore, surfaces with smaller asperities should hold larger droplets. However, conditions for the stability of the meniscus[31] and the contact lines[32] near the perimeter of the drop significantly reduce the actual load-bearing capability, in the case of our nanofilm to micronewtons per square millimetre.

Although adhesive, our hydrophobic nanofilm can support large sessile drops in Cassie states, that is, suspended atop the nanorods. As the PPX nanorod surfaces are hydrophobic ($\theta \geq 90°$), the pressure required for water to penetrate the interstitial regions scales as $\gamma/(\text{nanorod spacing})$[26]. As droplet pressure scales as γ/R and the droplet radius, R, is much larger than the ∼40 nm nanorod
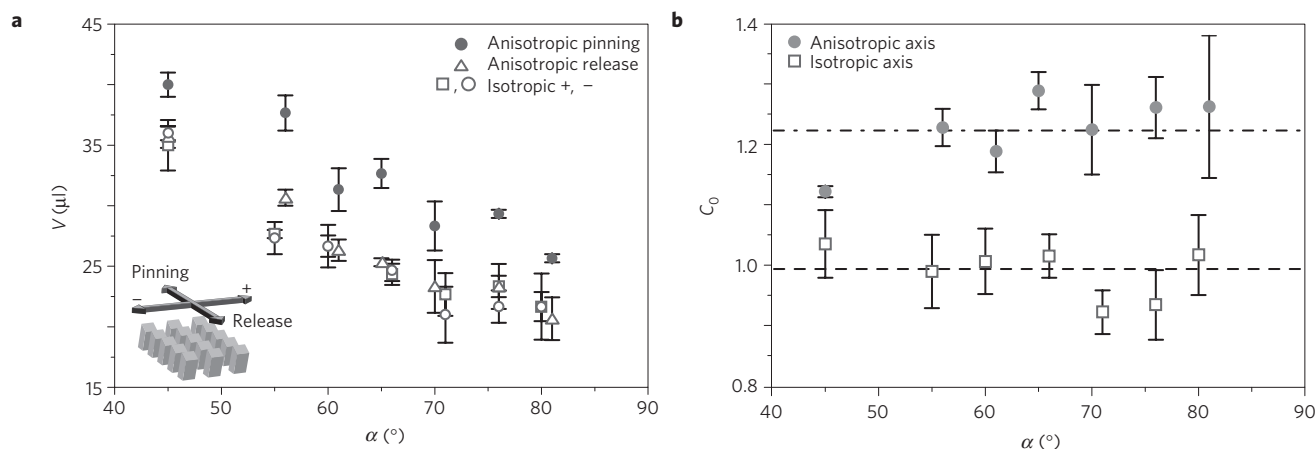
Figure 2 | Anisotropic wetting property of a PPX nanofilm. a, Critical drop volumes as functions of the substrate tilt angles α for the release (V_{REL}), pinning (V_{PIN}) and isotropic ($V_{ISO+,-}$) directions defined in the inset. **b**, The ratios V_{PIN}/V_{REL} and V_{ISO+}/V_{ISO-} as functions of α. The averages of each data set (dashed lines) agree well with our theoretical model. The error bars indicate the standard deviation.

separations, penetration is negligible. Thus, drops remain in a Cassie state atop the nanorods.

The anisotropic wetting of our PPX nanofilm is quantified by the critical droplet volume V that can adhere to the nanofilm tilted at an angle α. Tilting our nanofilm at an angle α relative to the horizontal imparts a downslope gravitational force of magnitude $F_g = \rho g V \sin \alpha$ on the drop, where V is the drop volume, ρ is the density of water and g is the gravitational acceleration, that opposes the retention force F_r. For a given tilt angle α, the drop volume V may be increased until the two forces are equal and opposite and the drop is on the verge of motion. Drop volume is measured in Fig. 2a in the release (V_{REL}), pinning (V_{PIN}) and isotropic ($V_{ISO+,-}$) directions for various tilt angles. Figure 2a shows that the critical drop volumes for the pinning direction are larger than those for the release and isotropic directions for tilt angles between 40° and 80°. The ratio of V_{PIN} to V_{REL} ranges from 1.12 to 1.29, with an average of 1.22 ± 0.06 (Fig. 2b). In contrast, we do not observe significant wetting anisotropy in the isotropic direction. The ratio of critical drop volumes V_{ISO+}/V_{ISO-} ranges from 0.92 to 1.04, with an average of 0.99 ± 0.04. A simple calculation of the retention force, which equals the critical gravitational force required for incipient drop motion, $F_r = \rho V g \sin \alpha$, shows that the retention force in the pinning direction is up to 80 μN higher than in the release direction, over ten times greater than the values reported for other engineered anisotropic surfaces[16].

Time-lapse frames of droplet motion on PPX nanofilm coated and uncoated half-pipes are shown in Fig. 3. A glass tube was cut in half along its centre axis. The inner surface of the resulting half-pipe was coated with the PPX nanofilm according to the protocols described in Methods, such that the longitudinal half-pipe axis was parallel to the anisotropic wetting direction of the PPX nanofilm. The other half-pipe was left uncoated (that is, a control). Both half-pipes were glued to a substrate, which was in turn mounted on a stage. Drops (5 μl) of water were placed at the centres of the coated and uncoated half-pipes and subjected to low-amplitude random vibrations (Methods). Water drops translated axially on the coated half-pipe, whereas those on the uncoated half-pipe merely vibrated randomly.

The anisotropic wetting response observed in Figs 1–3 is rationalized by a simple ratcheting model for pillared substrates. On the basis of the force of retention, the anisotropic adhesive wetting is derived from the directional dependence of the advancing and receding contact angles, θ_a and θ_r, of a droplet on the nanofilm. We estimate θ_a and θ_r by generalizing the approach of Extrand for

two-dimensional (2D) ratchets[5] and 3D vertical pillars[33]. Following Extrand's geometric argument, we introduce the linear fraction of the advancing or receding contact line on the pillars, λ, and approximate the contact angles θ_a and θ_r as linear averages of the contact angle the meniscus makes with a pillar and the 180° angle it makes with air. Simple geometry relates the contact angle between the advancing or receding meniscus and a pillar surface in terms of the intrinsic contact angles θ_{a0} and θ_{r0} of the material, the nanorod tilt angle β and diameter d, and the perpendicular spacing δ (Fig. 4). In the release direction, the advancing angle is $\theta_{aREL} = \lambda \min(\pi, \max(\theta_{a1}, \theta_{a2})) + (1-\lambda)\pi$, where $\theta_{a1} = 3\pi/2 - \beta - \arctan(\cot(\beta)/(1-s))$ (Fig. 4, case 1) and $\theta_{a2} = \theta_{a0} + \pi/2 - \beta$ (Fig. 4, case 2), and the receding angle is $\theta_{rREL} = \lambda(\theta_{r0} + \beta - \pi/2) + (1-\lambda)\pi$. We have defined the solid fraction in the longitudinal direction as $s = d/(d+\delta)$. In the pinning direction, $\theta_{aPIN} = \lambda \min(\pi, \theta_{a0} + \beta) + (1-\lambda)\pi$ and $\theta_{rPIN} = \lambda(\theta_{r0} - \beta) + (1-\lambda)\pi$. For a single droplet, the ratio of the retention forces in the pin and release directions is

$$\frac{F_{PIN}}{F_{REL}} = \frac{\cos\theta_{rPIN} - \cos\theta_{aPIN}}{\cos\theta_{rREL} - \cos\theta_{aREL}} \tag{1}$$

For the special case of a droplet running parallel to longitudinal ratcheted rails ($\delta = 0, s = 1$),

$$\frac{F_{PIN}}{F_{REL}} = \frac{\sin(\lambda(\beta + (1/2)\Delta\theta_0))}{\sin(\lambda(\pi/2 - \beta + (1/2)\Delta\theta_0))} \tag{2}$$

where $\Delta\theta_0 = \theta_{a0} - \theta_{r0}$ is the difference in the intrinsic advancing and receding contact angles of a flat surface of the material. For a 2D ratcheted grating ($\delta = 0, s = 1, \lambda = 1$), equation (2) reduces to Extrand's ratchet result derived from geometrical considerations[5]. For a droplet on a substrate of vertical pillars ($\beta = 90°$), the advancing and receding angles reduce to Extrand's vertical pillar results. For a given nanofilm, β, λ, s and $\Delta\theta_0 = \theta_{a0} - \theta_{r0}$ are fixed and measurable. Thus, equation (1) predicts that the ratio of the retention forces for a drop on the nanofilm will be a constant, C_0, as observed in our experiments. Moreover, as the retention force equals the critical gravitational force $\rho V g \sin \alpha$, we have

$$\frac{V_{PIN}R_{REL}\sin\alpha_{PIN}}{V_{REL}R_{PIN}\sin\alpha_{REL}} = \frac{\cos\theta_{rPIN} - \cos\theta_{aPIN}}{\cos\theta_{rREL} - \cos\theta_{aREL}} = C_0 \tag{3}$$

The factors of R originate from the equation for the retention force; we have neglected the changes in k due to droplet shape[28,34]. Assuming that R scales as $V^{1/3}$, then for a fixed

a

b
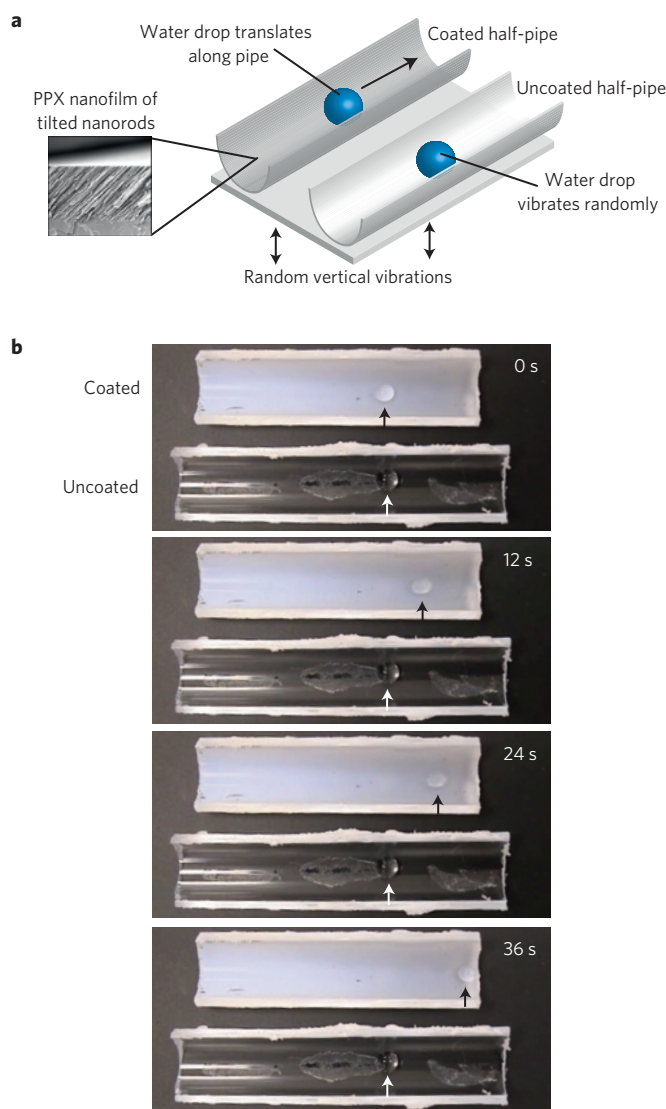
Figure 3 | Drop motion on a PPX nanofilm coated half-pipe. a, Schematic of experimental set-up. Two half-pipes, one coated with PPX nanofilm and the other uncoated, were glued to a base. Low-amplitude ~85 Hz random vibration of the base caused translational droplet motion on the coated half-pipe, but not on the uncoated pipe. **b**, Time-lapse of droplet motion in the coated and uncoated half pipes. Water drops translated axially on the half-pipe coated with PPX nanofilm, whereas those on the uncoated half-pipe merely vibrated randomly. Glue is visible beneath uncoated pipe; the surface is smooth and clean. The arrows indicate droplet position.

tilt angle α, $(V_{\mathrm{PIN}}/V_{\mathrm{REL}})^{2/3} = C_0$. Our PPX nanofilm consists of nanorods of diameter $d \sim 150$ nm, spacing $\delta \sim 40$ nm, solid fraction $s \sim 0.80$ and tilt $\beta = 55°$. We measured the intrinsic advancing and receding angles of a flat PPX coating as $\theta_{a0} = 95°$ and $\theta_{r0} = 75°$. Approximating our nanofilm as a square array of circular posts, $\lambda = \pi s/(2(1 + (\pi/2 - 1)s)) \cong 0.85$. With these parameter values, equation (3) gives $C_0 = 1.22$, close to the measured value $(V_{\mathrm{PIN}}/V_{\mathrm{REL}})^{2/3} = (1.22 \pm 0.06)^{2/3} = 1.14 \pm 0.04$. In the pinning direction, our model predicts the advancing and receding angles 154° and 43°, respectively, compared with the measured angles 132° and 47° ± 5°; in the release direction, the predictions are 147° and 60° compared with the measured values 128° and 60° ± 5°. The conclusion is that the receding angles are predicted much more accurately than the advancing angles, which should still yield reasonable estimates of the hysteresis because of the mild

a Advancing and receding edge of forced drop

b Release direction

c Pin direction
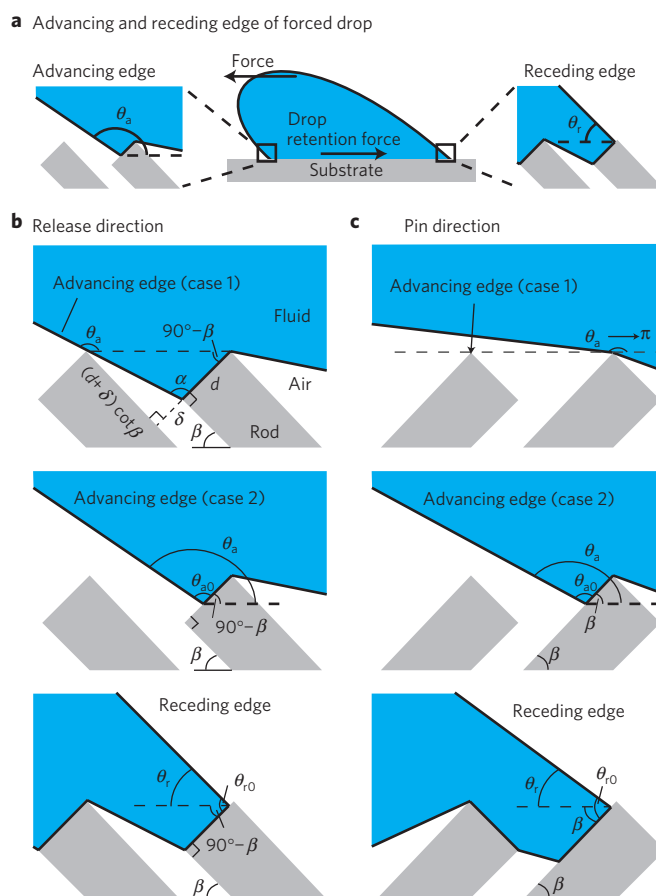
Figure 4 | Model of advancing and receding contact angles. a, Schematic of drop and its advancing and receding edges on a textured surface. **b,c**, Geometry of contact between the drop and roughness elements when the drop is forced in the release (**b**) and the pinning (**c**) directions. For the drop to advance in either direction, its advancing edge must contact the next roughness element (case 1) and move along the roughness top (case 2). The macroscopic contact angles θ_a and θ_r between the advancing and receding menisci and the substrate axis are functions of the intrinsic contact angles θ_{a0} and θ_{r0} of the material, the nanorod tilt angle β and diameter d, and the perpendicular spacing δ. Note that the substrate constrains θ_a and θ_r to be between 0 and 180°.

slope of the cosine function near 180°. Moreover, the differences in hysteresis approximately cancel when calculating the ratio C_0. The agreement between model and experiment is encouraging, given the modelling simplifications and variations associated with PPX non-uniformities, evaporative losses, especially important for smaller drops, and spurious mechanical vibrations that promote drop release, some of which are discussed further below.

The capillary forces experienced by the thin nanorods can cause deflection and alter the spacing of the nanorod tips. In particular, nanorods may clump near the drop perimeter[18], reducing the local tip spacing to zero. This observation is consistent with the large ratio of capillary force to beam bending resistance, $\sim h^2 \gamma d/(EI) \sim 870$, where the nanorod moment of inertia is $I = \pi d^4/64$, diameter $d \sim 150$ nm, length $h \sim 10$ μm and Young's modulus $E \sim 50$ MPa (ref. 17). Despite the possible variations in tip spacing, our model gives similar predictions: zero tip spacing ($s = 1$) at the receding edge increases our prediction of C_0 from 1.22 to 1.32, still close to our measured values.

Having characterized and rationalized the unidirectional adhesive nature of our nanofilm, we now consider its control. Our model suggests that unidirectional adhesion, as quantified by C_0, may be

controlled by adjusting column tilt angle β, the intrinsic parylene contact angles $(\theta_{a0}, \theta_{r0})$ and the nanorod arrangement (λ, s). At present, β can be varied only between 55° and 65°. Increasing β to 65° increases the predicted C_0 from 1.22 to 1.50. Surface treatments such as those listed above also allow the intrinsic contact angles to be varied. For example, increasing the intrinsic contact angles $(\theta_{r0}, \theta_{a0})$ from $(75°, 95°)$ to $(85°, 105°)$ increases the predicted C_0 from 1.22 to 1.31. Last, increasing the perpendicular space between nanorods from 40 nm to 100 nm increases the predicted C_0 from 1.22 to 1.49, and decreasing the spacing to zero $(d = \delta, \lambda = 1, s = 1,$ that is, Extrand's result) also increases C_0 from 1.22 to 1.28. Note that C_0 increases with $s = d/(d + \delta)$, but decreases as λ increases, as illustrated in additional plots in Supplementary Fig. S2.

Although the nanofilm design parameters allow us to control its wetting properties, their variation across the nanofilm naturally leads to variations in adhesive wetting behaviour. Variations in nanofilm structure are evident in the scanning electron micrograph in Fig. 1b. Changes in rod diameter could occur during growth because of radical flux fluctuations and/or defect sites in the growing rods. In addition, the shadowing effects that dominate rod growth produce rods with distorted rounded tips and a distribution of rod heights. Although these variations are evident in observations of critical volume, the adhesive force in the pin direction is always significantly larger than that in the other directions. Therefore, these variations do not affect the unidirectional nature of the adhesive force, important for applications involving unidirectional droplet propulsion. This is not surprising, as our calculations indicate that the directional adhesion quantified by C_0 varies smoothly (and modestly) over all the parameter values in the regime of interest.

Although our work has focused on hydrophobic surfaces with anisotropic wetting, other related anisotropic surfaces exist with unique properties. The geometry and motion of the beaks of certain birds allow them to propel droplets into their beaks[35]. This mechanism has inspired tapered tubes and mechanical beaks that propel droplets[35,36]. Also, hydrophilic surfaces with anisotropic wetting can control the extent and shape of the wetted area[37,38].

We have reported an engineered nanofilm that possesses a pin-release droplet ratchet mechanism derived from nanoscale asperities. We have outlined a simple preparation method that produces nanofilms exhibiting 80 µN differences in the droplet retention forces in the pin and release directions, and a microscale smooth surface on which to transport microlitre droplets. We emphasize that our film properties stem from the unique chemical, mechanical and morphological characteristics of our PPX material. An accompanying model provides reasonable predictions of the observed wetting behaviour and elucidates the values of key design parameters required to enhance the anisotropic adhesion. Ongoing work includes optimizing the droplet transport mechanism and tuning the preparation method to engineer droplet pathways and other pin-release surfaces with complex geometries and surface treatments. Our nanofilm with unidirectional wetting is potentially useful for a wide range of applications, including digital microfluidic devices, drag reduction for antifouling surfaces and biomedical coating applications.

Methods

Film deposition. Deionized water of 18.2 MΩ cm (Barnstead Nanopure Diamond dispenser) was used for all experiments. p-type Si(100) wafers (Wafernet) were used as substrates for PPX nanofilm deposition. Si(100) wafers were cleaned and a self-assembled monolayer (SAM) of allyltrimethoxysilane (Gelest) was deposited per the procedure used in our previous work[23]. SAM-functionalized wafers were stored in a dark container at a temperature of 4 °C until required for the polymer deposition. For PPX nanofilm deposition, we modified Gorham's deposition method for PPX films using a low-pressure, vapour deposition technique. Dichloro-[2,2]-paracyclophane (PDS) was used as the precursor for PPX nanofilm deposition. 0.3 g of the precursor was sublimed at a temperature of 175 °C under a pressure of ∼10 torr. The precursor vapour was then pyrolysed at 690 °C. The pyrolysis of dichloro-[2,2]-paracyclophane results in the cleavage of the alkyl bridge

to form chloro-p-quinodimethane (or chloro-p-xylylene) diradical. The diradical flux when directed at an angle of 10° on the silicon substrate results in a low-density porous PPX film with aligned nanorod morphology[23].

Characterization. Field-emission scanning electron microscope (FESEM) images of the film surface were taken using a FESEM (JEOL 6700F) operated at 3 kV accelerating voltage. Contact angles were measured with a contact angle instrument (FTA 1000B, First Ten Angstroms) equipped with a rotatable stage and video camera. Distilled water droplet volumes were increased until the drops no longer adhered to the tilted nanofilm. The experiments were repeated at least three times in different locations on the PPX substrate using a fresh dry PPX substrate for each experiment. The experiments were carried out at room temperature without controlling relative humidity.

Drop transport. The drop transport videos (Supplementary Videos) and extracted frames shown in Fig. 3 demonstrate the use of our PPX anisotropic nanofilm for drop transport. Vibrations were imparted to the substrate by means of a vibrator (PASCO Mechanical Vibrator-SF 9,324) at low amplitude (Supplementary Fig. S3) at ∼85 Hz. Drop motion was recorded with a Samsung HMX-H106 digital camcorder. Under random vibration, drops always moved from left to right in the PPX coated half-pipe, compared with the random motion in the uncoated tube. The same results were obtained in any repeated experiments, demonstrating the unidirectional nature of the PPX nanofilm.

Computation. All theoretical estimates in the Article, and the plots in Supplementary Fig. S2, were made by programming equation (3) and the formulae for the advancing and receding contact angles into a Mathematica notebook, included with the Supplementary Information.

References

1. Huber, G. *et al.* Evidence for capillarity contributions to gecko adhesion from single spatula nanomechanical measurements. *Proc. Natl Acad. Sci. USA* **102,** 16293–16296 (2005).
2. Bush, J. W. M., Hu, D. L. & Prakash, M. The integument of water-walking arthropods: Form and function. *Adv. Insect Physiol.* **34,** 117–192 (2007).
3. Zheng, Y. M., Gao, X. F. & Jiang, L. Directional adhesion of superhydrophobic butterfly wings. *Soft Matter* **3,** 178–182 (2007).
4. Oelschlägel, B., Gorb, S., Wanke, S. & Neinhuis, C. Structure and biomechanics of trapping flower trichomes and their role in the pollination biology of Aristolochia plants (Aristolochiaceae). *New Phytol.* **184,** 988–1002 (2009).
5. Extrand, C. W. Retention forces of a liquid slug in a rough capillary tube with symmetric or asymmetric features. *Langmuir* **23,** 1867–1871 (2007).
6. Berthier, J. *Microdrops and Digital Microfluidics* (William Andrew, 2008).
7. Pesika, N. S. *et al.* Gecko adhesion pad: A smart surface? *J. Phys. Condens. Matter* **21,** 464132 (2009).
8. Mahdavi, A. *et al.* A biodegradable and biocompatible gecko-inspired tissue adhesive. *Proc. Natl Acad. Sci. USA* **105,** 2307–2312 (2008).
9. de Gennes, P-G., Brochard-Wyart, F. & Quéré, D. *Capillarity and Wetting Phenomena: Drops, Bubbles, Pearls, Waves* (Springer, 2004).
10. Khoo, H. S. & Tseng, F. G. Spontaneous high-speed transport of subnanoliter water droplet on gradient nanotextured surfaces. *Appl. Phys. Lett.* **95,** 063108 (2009).
11. Ichimura, K., Oh, S-K. & Nakagawa, M. Light-driven motion of liquids on a photoresponsive surface. *Science* **288,** 1624–1626 (2000).
12. Daniel, S., Sircar, S., Gliem, J. & Chaudhury, M. K. Ratcheting motion of liquid drops on gradient surfaces. *Langmuir* **20,** 4085–4092 (2004).
13. Sandre, O., Gorre-Talini, L., Ajdari, A., Prost, J. & Silberzan, P. Moving droplets on asymmetrically structured surfaces. *Phys. Rev. E* **60,** 2964–2972 (1999).
14. Shastry, A., Case, M. J. & Böhringer, K. F. Directing droplets using microstructured surfaces. *Langmuir* **22,** 6161–6167 (2006).
15. Linke, H. *et al.* Self-propelled Leidenfrost droplets. *Phys. Rev. Lett.* **96,** 154502 (2006).
16. Zhang, J., Cheng, Z., Zheng, Y. & Jiang, L. Ratchet-induced anisotropic behavior of superparamagnetic microdroplet. *Appl. Phys. Lett.* **94,** 144104 (2009).
17. So, E., Demirel, M. C. & Wahl, K. J. Mechanical anisotropy of nanostructured parylene films during sliding contact. *J. Phys. D* **43,** 045403 (2010).
18. Demirel, M. C., Cetinkaya, M., Singh, A. & Dressick, W. J. Noncovalent deposition of nanoporous Ni membranes on spatially organized poly(p-xylylene) film templates. *Adv. Mater.* **19,** 4495–4499 (2007).
19. Malvadkar, N. A., Sekeroglu, K., Dressick, W. J. & Demirel, M. C. Noncovalent mechanism for the conformal metallization of nanostructured parylene films. *Langmuir* **26,** 4382–4391 (2010).
20. Malvadkar, N. A., Dressick, W. J. & Demirel, M. C. Liquid phase deposition of titania onto nanostructured poly-p-xylylene thin films. *J. Mater. Chem.* **19,** 4796–4804 (2009).

21. Malvadkar, N. A., Park, S., Urquidi-MacDonald, M., Wang, H. & Demirel, M. C. Catalytic activity of cobalt deposited on nanostructured poly(*p*-xylylene) films. *J. Power Sources* **182**, 323–328 (2008).
22. Demirel, M. C. *et al.* Bio-organism sensing via surface enhanced Raman spectroscopy on controlled metal/polymer nanostructured substrates. *Biointerphases* **4**, 35–41 (2009).
23. Boduroglu, S., Cetinkaya, M., Dressick, W. J., Singh, A. & Demirel, M. C. Controlling the wettability and adhesion of nanostructured poly-(*p*-xylylene) films. *Langmuir* **23**, 11391–11395 (2007).
24. Lee, W. *et al.* Nanostructure-dependent water-droplet adhesiveness change in superhydrophobic anodic aluminum oxide surfaces: From highly adhesive to self-cleanable. *Langmuir* **26**, 1412–1415 (2010).
25. Cheng, Z., Gao, J. & Jiang, L. Tip geometry controls adhesive states of superhydrophobic surfaces. *Langmuir* **26**, 8233–8238 (2010).
26. Quéré, D. Wetting and roughness. *Ann. Rev. Mater. Res.* **38**, 16.1–16.29 (2008).
27. Dussan V, E. B. & Chow, R. T-P. On the ability of drops or bubbles to stick to non-horizontal surfaces of solids. *J. Fluid Mech.* **137**, 1–29 (1983).
28. Extrand, C. W. & Kumagai, Y. Liquid drops on an inclined plane: The relation between contact angles, drop shape, and retentive force. *J. Colloid Interface Sci.* **170**, 515–521 (1995).
29. Nadkarni, G. D. & Garoff, S. An investigation of microscopic aspects of contact angle hysteresis: Pinning of the contact line on a single defect. *Europhys. Lett.* **20**, 523–528 (1992).
30. de Gennes, P. G. Wetting: Statics and dynamics. *Rev. Mod. Phys.* **57**, 827–863 (1985).
31. Michael, D. H. Meniscus stability. *Ann. Rev. Fluid Mech.* **13**, 189–216 (1981).
32. Gao, L. & McCarthy, T. J. Wetting 101°. *Langmuir* **25**, 14105–14115 (2009).
33. Extrand, C. W. Model for contact angles and hysteresis on rough and ultraphobic surfaces. *Langmuir* **18**, 7991–7999 (2002).
34. ElSherbini, A. I. & Jacobi, A. M. Retention forces and contact angles for critical liquid drops on non-horizontal surfaces. *J. Colloid Interface Sci.* **299**, 841–849 (2006).
35. Prakash, M., Quéré, D. & Bush, J. W. M. Surface tension transport of prey by feeding shorebirds: the capillary ratchet. *Science* **320**, 931–934 (2008).
36. Renvoisé, P., Bush, J. W. M., Prakash, M. & Quéré, D. Drop propulsion in tapered tubes. *Europhys. Lett.* **86**, 64003 (2009).
37. Courbin, L. *et al.* Imbibition by polygonal spreading on microdecorated surfaces. *Nature Mater.* **6**, 661–664 (2007).
38. Chu, K. H., Xiao, R. & Wang, E. N. Uni-directional liquid spreading on asymmetric nanostructured surfaces. *Nature Mater.* **9**, 413–417 (2010).

Author contributions

M.C.D. and W.J.D. planned the research, and M.C.D. supervised the research. M.C.D., N.A.M. and K.S. carried out the experiments. M.J.H. developed the theoretical model. All authors contributed to writing and revising the manuscript, and agreed on its final contents.

Additional information

The authors declare no competing financial interests. Supplementary information accompanies this paper on www.nature.com/naturematerials. Reprints and permissions information is available online at http://npg.nature.com/reprintsandpermissions. Correspondence and requests for materials should be addressed to M.C.D.